analytical chemistry

Article

Cite This: *Anal. Chem.* 2019, 91, 12453−12460

pubs.acs.org/ac

A Metal−Organic Framework as Selectivity Regulator for Fe^{3+} and Ascorbic Acid Detection

Lan Guo,[†] Yuan Liu,[‡] Rongmei Kong,[†] Guang Chen,[†] Zhe Liu,[†] Fengli Qu,[*,†] Lian Xia,[*,†] and Weihong Tan[‡]

[†]Key Laboratory of Life-Organic Analysis of Shandong Province, Qufu Normal University, Qufu, P. R. China

[‡]Center for Research at Bio/Nano Interface, Department of Chemistry and Department of Physiology and Functional Genomics, Health Cancer Center, UF Genetics Institute and McKnight Brain Institute, University of Florida, Gainesville, Florida 32611-7200, United States

Supporting Information

ABSTRACT: Ferric ion (Fe^{3+}) plays a vital role in cellular homeostasis. However, the detection of Fe^{3+} with rhodamine B (RhB) has potential problems, such as poor selectivity and low photostability. To address these problems, we rationally designed an RhB@MOF nanocomposite-based "on−off−on" fluorescent switching nanoprobe for highly sensitive and selective detection of Fe^{3+} and ascorbic acid. This RhB@MOF nanoprobe was prepared through a facile one-pot synthesis. Here MOF served as a selectivity regulator for the detection of Fe^{3+}. By embedding RhB into the porous crystalline MOF, enhanced photostability and fluorescence lifetime of RhB to Fe^{3+} were achieved. The as-prepared RhB@MOF was demonstrated to be an ultrasensitive and selective nanoprobe for the detection of Fe^{3+} in human serum and ascorbic acid in rat brain microdialysate. Furthermore, inner filter effect (IFE) and photoinduced electron transfer (PET) were proposed and discussed to explain the selectivity and sensitivity of RhB to Fe^{3+} against other interfering substances. Our novel "on−off−on" nanoprobe provides insight into the rational design of MOF-based biosensors for selective and sensitive detection of analytes.

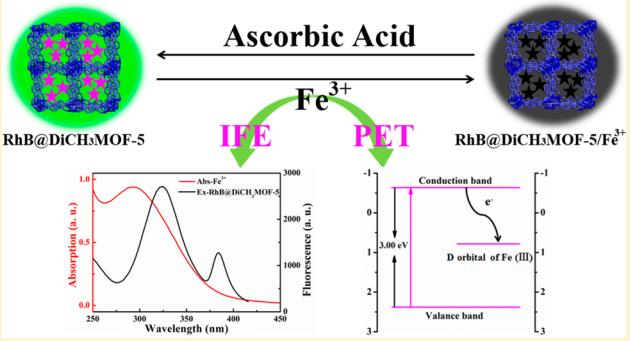

Ferric ion (Fe^{3+}), as one of the inorganic transition metal ions, plays a vital role in physiological processes, with clinical and environmental implications.[1] Both excess and deficiency of Fe^{3+} can destabilize cellular homeostasis and lead to various diseases, such as iron deficiency anemia (IDA), arthritis, liver injury, renal failure, diabetes, Parkinson's and Alzheimer's diseases, and even cancers.[2−4] Hence, determination of Fe^{3+} is key to the early diagnosis of these diseases. Among various detection strategies, fluorescence-based methods have attracted increased attention because of their high sensitivity, diverse selectivity, and easy operation.[5−7] Over the last few decades, rhodamine B (RhB) and its derivatives have been used for Fe^{3+} detection owing to their photophysical properties, such as high molar extinction coefficient and inertness to pH, as well as high fluorescence quantum yield.[8−11] However, RhB-based sensors intrinsically suffer from poor selectivity and low photostability as a result of interference with other trivalent metal ions, especially Cr^{3+}, and tedious functional group modification, as well as short fluorescence lifetime.[1,8] To overcome the shortcomings of organic dye-based detection of Fe^{3+}, some researchers developed inorganic nanoparticle-based sensors, such as carbon dots (CDs) and semiconductor quantum dots (SQDs).[12−15] These inorganic nanoscale dots possess outstanding properties, including good photostability, excellent biocompatibility, and cell membrane permeability based on their small size, tunable surface functionality, and long-term resistance to photobleaching. Despite the highly anticipated potential of these nanosensors, some issues, including short-wavelength emission, small Stokes shift, low quantum yield, and poor selectivity, have limited their applications in Fe^{3+} detection. Recently, metal−organic frameworks (MOFs) have attracted attention for their unique physicochemical properties.[16−24] Luminescent porous MOF-based sensors not only have nanoscale cavities but also show three-dimensional (3D) network architectures. These nanoscale cavities can act as microreactors, which offer sufficient space for the recognition and selective detection of guest targets. In addition, their 3D network structure promotes exciton migration over the framework and improves detection sensitivity through signal amplification. For instance, Yan and co-workers have successfully employed MIL (Materials Institute of Lavoisier)-53(Al) for the detection of Fe^{3+} based on cation exchange between the framework metal ion Al^{3+} in MIL-53(Al) and

Received: July 11, 2019
Accepted: August 30, 2019
Published: August 30, 2019

DOI: 10.1021/acs.analchem.9b03143
Anal. Chem. 2019, 91, 12453−12460

Fe^{3+}.[25] However, such ion exchange involved a prolonged process resulting in attenuating the efficiency and applicability of this detection method. Fluorescent organic linkers- or lanthanide element-based emissions, such as Ce^{4+}, Tb^{3+}, or Eu^{3+}, were other main sources of luminous characteristics of MOFs.[26−33] Acting as host matrixes, MOFs provide a distinct platform to stabilize and confine functional species, leading to specific behavior inside the defined pore environments. Immobilization of organic dyes into the pore spaces of MOFs can minimize aggregation-caused quenching. Thus, MOF@organic dye composites combine the crystalline benefit of MOFs and luminescent behavior of organic dyes. Based on the superior features of porous crystalline MOFs, the development of MOF-based host−guest probes for Fe^{3+} detection with high selectivity and sensitivity remains a goal.

Therefore, we herein report an innovative sensor constructed by embedding the fluorescent dye RhB into porous microcrystalline Zn(II)-MOF (RhB@DiCH$_3$MOF-5) through a facile one-pot synthesis approach for Fe^{3+} detection. The RhB@DiCH$_3$MOF-5 composite features a green-yellow emission at 552 nm derived from RhB when dispersed in aqueous solution; however, improved photostability and longer fluorescence lifetime were observed compared with free RhB. Furthermore, loading RhB into the porous crystalline DiCH$_3$MOF-5 enables RhB to selectively quench Fe^{3+}. Moreover, this as-synthesized RhB@DiCH$_3$MOF-5 can be applied to a dual-detection of Fe^{3+} and ascorbic acid through an "on−off−on" fluorescence response. As shown in Scheme 1,

Scheme 1. Synthesis of Highly Fluorescent RhB@DiCH$_3$MOF-5 Composites and Their Application in Fe^{3+} and Ascorbic Acid Detection

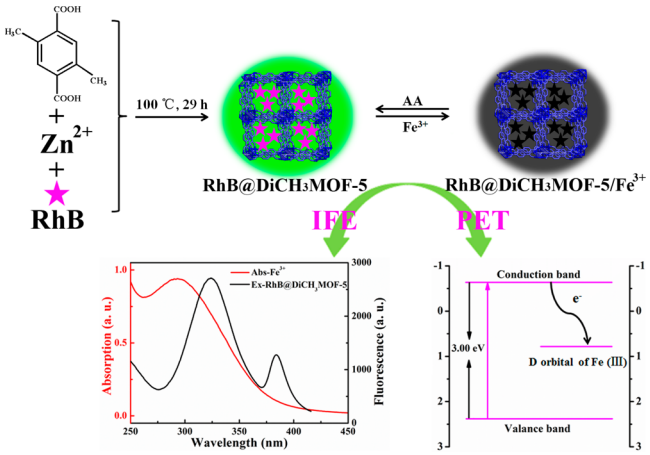

the luminescent intensity is significantly decreased upon adding Fe^{3+} owing to the synergism of inner filter effect (IFE) and photoinduced electron transfer (PET). However, after ascorbic acid was introduced to the quenched solution, the fluorescence of RhB@DiCH$_3$MOF-5 recovered. This fluorescence recovery could be attributed to an oxidation−reduction reaction. The established sensor platform was then successfully employed for the determination of Fe^{3+} in human serum samples and ascorbic acid in rat brain microdialysates.

■ EXPERIMENTAL SECTION

Materials and Methods. All reagents and solvents were commercially available and used as received without purification. The fluorescence spectra were recorded with a Hitachi F-7000 fluorescence spectra photometer (Tokyo, Japan) with test parameters as follows: emission and excitation slit widths were all 10 nm, photomultiplier voltage was 700 V, and scan speed was 1200 nm min^{-1}. X-ray diffraction (XRD) patterns were performed using the Panalytical X-ray Diffractometer Model X pert3 employing Cu Kα radiation (λ = 1.5406 Å). Scanning electron microscopy (SEM) images were obtained by the JSM-6700F scanning electron microscope. The fluorescence lifetime measurements were recorded by FLS980 series of fluorescence spectrometers.

Synthesis of DiCH$_3$MOF-5 and RhB@DiCH$_3$MOF-5 Composites. DiCH$_3$MOF-5 was synthesized following the previously reported method with some modifications.[34] A mixture of 4 mL of a $Zn(NO_3)_2{\cdot}6H_2O$ solution in diethylformamide (DEF) (0.3 mol L^{-1}) and 4 mL 2,5-dimethylterephthalic acid solution in DEF (0.1 mol L^{-1}) was put into a 20 mL glass screw-capped vial and sealed before placing in an oil bath (100 °C) for 29 h. After crystallization, the suspensions were collected using centrifugation (7000 rpm, 5 min) and washed with DEF several times. Then the crystals were immersed in $CHCl_3$ (4 mL) for 24 h (3×). The solvent-exchanged product was heated at 160 °C in vacuum for 24 h. Dye-encapsulated MOF composites (RhB@DiCH$_3$MOF-5) were parallelly prepared using the same conditions with that of DiCH$_3$MOF-5, except that RhB (0.01 mol L^{-1}) was added into the precursor solution of DiCH$_3$MOF-5.

Quantification of Fe^{3+} and Ascorbic Acid Using RhB@DiCH$_3$MOF-5 Composites. The detection of Fe^{3+} was performed in NaAc−HAc buffer (10 mmol L^{-1}, pH 6.0) at room temperature. In a typical run, standard stock solution of RhB@DiCH$_3$MOF-5 was obtained by dispersing 5.0 mg of RhB@DiCH$_3$MOF-5 powder in 100 mL of deionized water under ultrasonic conditions for 10 min. Subsequently, 100 μL of RhB@DiCH$_3$MOF-5 stock solution was mixed with 100 μL of different concentrations of Fe^{3+} solution and 800 μL of NaAc-HAc buffer (10 mmol L^{-1}, pH 6.0). The resulting solution was mixed thoroughly before measuring the fluorescence emission spectra in a quartz cell with excitation at 325 nm.

To determine the concentration of ascorbic acid, 100 μL of Fe^{3+} (0.5 mmol L^{-1}) was introduced into RhB@DiCH$_3$MOF-5 (100 μL, 50 mg L^{-1}) to form a sensitive and selective fluorescent sensing platform denoted as RhB@DiCH$_3$MOF-5/Fe^{3+}. Then 100 μL of various concentrations of ascorbic acid was added, and the resulting mixture was shaken thoroughly. After incubation at room temperature for 30 min, fluorescence recovery spectra were recorded. The selectivity of RhB@DiCH$_3$MOF-5/Fe^{3+} probe to ascorbic acid was evaluated by adding some other interference substances containing L-alanine (L-Ala), L-cysteine (L-Cys), L-glutathione (GSH), L-serine (L-Ser), L-tryptophan (L-Try), L-tyrosine (L-Tyr), L-valine (L-Val), DL-phenylalanine (DL-Phe), homocysteine (Hcy), glucose (Glu), citric acid (CA), and tartaric acid (TA) respectively, in a manner similar to that of ascorbic acid.

Analysis of Real Samples. The human serum samples were obtained from Qufu People's Hospital, and all experiments were carried out according to the relevant laws and regulations. Serum samples were diluted 100-fold before analysis, and the diluted samples were added with different concentrations of standard Fe^{3+} solution.

Animal studies were carried out with the approval of Qufu Normal University Animal Care Committee. Microdialysis experiments in vivo were performed as reported previ-

DOI: 10.1021/acs.analchem.9b03143
Anal. Chem. 2019, 91, 12453−12460

ously.[35−38] In short, after being equipped the with guide cannula, the rats were anesthetized using chloral hydrate (350 mg kg^{-1} ip). The microdialysis needle with a length of 2 mm was then implanted into the striatum of the rats' brain cortex area situated 2.5 mm fore from bregma, 2.5 mm from midline sidewise, and 7.0 mm under dura. The device was filled in artificial cerebrospinal fluid (126 mmol L^{-1} NaCl, 2.4 mmol L^{-1} KCl, 1.1 mmol L^{-1} $CaCl_2$, 0.85 mmol L^{-1} $MgCl_2$, 27.5 mmol L^{-1} $NaHCO_3$, 0.5 mmol L^{-1} Na_2SO_4, 0.5 mmol L^{-1} KH_2PO_4, pH 7.0) with 3 μL min^{-1} velocity of flow driven by a microinjection pump. Then every 0.1 mL of rat brain dialysate was collected when balanced for at least 90 min. All the samples were used directly without any treatments.

Energy Level Calculation of RhB@DiCH$_3$MOF-5 Cyclic Voltammetry. Cyclic voltammetry measurements were carried out on a CHI 760E electrochemical workstation to test the valence band of RhB@DiCH$_3$MOF-5. All experiments were performed at room temperature using a conventional three-electrode system: MOFs-coated glassy carbon (Φ = 3 cm) working electrode, a Pt wire as counter electrode, and an Ag/AgCl/sat. KCl electrode as the reference electrode. Measurements were carried on 10 mmol L^{-1} HAc−NaAc buffered solution as a supporting electrolyte in a nitrogen atmosphere. Oxidation potential of RhB@DiCH$_3$MOF-5 was determined in the windows of 0−3.0 V.

■ RESULTS AND DISCUSSION

Characterization of RhB@DiCH$_3$MOF-5 Composites. The synthesized sensing materials were first characterized by XRD. As shown in Figure 1A, the XRD patterns of the prepared DiCH$_3$MOF-5 and RhB@DiCH$_3$MOF-5 have good consistency with the simulated MOF-5, revealing that the two MOFs had been successfully synthesized. In particular, the sharp diffractions of RhB@DiCH$_3$MOF-5 were the same as those of pristine DiCH$_3$MOF-5, indicating that the encapsulation of RhB did not affect the structure or crystallinity of the main frameworks. The high crystallinity suggests the high quality and stability of the prepared materials in this work.

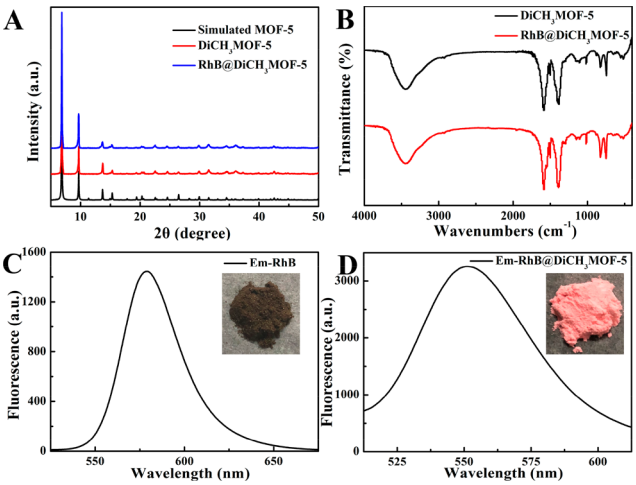

Figure 1. (A) XRD images of DiCH$_3$MOF-5, RhB@DiCH$_3$MOF-5, and simulated MOF-5. (B) FT-IR spectra of DiCH$_3$MOF-5 (black) and RhB@DiCH$_3$MOF-5 (red). (C) Fluorescence emission spectrum of dilute RhB dye solution. Inset shows the photo of RhB solid powder. (D) Fluorescence emission spectrum of RhB@DiCH$_3$MOF-5. Inset shows the photo of RhB@DiCH$_3$MOF-5 solid powder.

Figure 1B shows the FT-IR spectrum obtained from the prepared materials. The strong peak situated at 1380 cm^{-1} can be ascribed to the symmetrical stretching vibration of the carboxyl group which is one of the chief functional groups of BDC ligands. Also, the asymmetric stretching vibrations of the carboxyl groups are reflected in the other peak located at 1590 cm^{-1}. Moreover, no obvious change was observed in the FT-IR spectrum between DiCH$_3$MOF-5 and RhB@DiCH$_3$MOF-5, indicating the successful encapsulation of RhB into the pores of DiCH$_3$MOF-5. The porosity of DiCH$_3$MOF-5 and RhB@DiCH$_3$MOF-5 were confirmed by nitrogen sorption−desorption isotherms at 77 K, and the results are shown in Figure S1. As shown in Figure S1, the adsorption volume increases sharply with the pressure increasing at low pressure stage, whereas with a further increase in pressure after this, the adsorption isotherm is almost flat. According to the curve shape classified by the IUPAC classification, this sorption−desorption process showed typical type-I characteristics, which implied that the microporous characters of the two materials. The Brunauer−Emmett−Teller (BET) surface area of DiCH$_3$MOF-5 and RhB@DiCH$_3$MOF-5 were calculated to be 1690.8 m^2 g^{-1} and 1296.3 m^2 g^{-1}, respectively. The slightly less N_2 uptake capacity for RhB@DiCH$_3$MOF-5 than for DiCH$_3$MOF-5 might be attributed to the encapsulation of RhB. The large surface area contributes to the enhanced adsorption of analytes from liquid solution. The average pore size of DiCH$_3$MOF-5 is about 1.6 nm, which matches well with the molecular size of RhB (Figure S2), facilitating immobilization of RhB into the pore channels of DiCH$_3$MOF-5. To demonstrate the integration of dyes and MOFs, a contrast of RhB solution and RhB@DiCH$_3$MOF-5 dispersed in DEF solution was conducted before and after centrifugation. As anticipated, the supernatant of RhB@DiCH$_3$MOF-5 after centrifugation was clear and transparent, whereas the free RhB solution had no obvious changes, revealing that RhB was firmly loaded into DiCH$_3$MOF-5 (Figure S3). Furthermore, the absorbance of RhB at 550 nm was significantly decreased after loading into DiCH$_3$MOF-5 (Figure S4). Only a negligible shift in peak was observed, indicating that the absorbance of RhB was covered by DiCH$_3$MOF-5.[17]

SEM patterns in Figure S5A describe the "cube-sugar-like" morphology of the synthesized DiCH$_3$MOF-5, which is consistent with the results from the literature.[39] Figure S5B shows the morphology of RhB@DiCH$_3$MOF-5. Comparing Figure S5A and Figure S5B, we can see that the morphology of RhB@DiCH$_3$MOF-5 is same as that of DiCH$_3$MOF-5, which further proves that RhB molecules are fixed in the pores of DiCH$_3$MOF-5 and do not affect its structure. Moreover, the average side-length of DiCH$_3$MOF-5 or RhB@DiCH$_3$MOF-5 is approximately 1.4 μm, according to the measurement. The insets in Figure S5 indicate that DiCH$_3$MOF-5 and RhB@DiCH$_3$MOF-5 are uniform crystals decorated with a few nanoscale subcrystals.

Photoluminescence Studies of RhB@DiCH$_3$MOF-5. Characterization of RhB@DiCH$_3$MOF-5 indicated that the molecules of RhB were successfully embedded in the pores of DiCH$_3$MOF-5 and were well interspersed owing to the uniform pore confinement effect. Nonradiative energy transfer, which usually exists in aggregated dye molecules and leads to quenching of the dye emission, is inhibited in this superior structure. Especially, the luminescent behavior of RhB embedded in DiCH$_3$MOF-5 is analogous to that of dilute RhB dye (Figure 1C and Figure 1D), further proving a good

DOI: 10.1021/acs.analchem.9b03143
Anal. Chem. 2019, 91, 12453−12460

dispersion of the incorporated RhB. Upon encapsulation, the emission spectrum presents a certain degree of blue shift, which was associated with the increased rigidity, dye deprotonation, and more importantly the reduced quenching caused by dye aggregation.[40,41] In addition, the fluorescence emission of RhB@DiCH$_3$MOF-5 in different pH solutions was steady, thus benefiting fluorescent applications in difficult conditions (Figure S6A). As shown in Figure S6B, the XRD patterns of ultrasonicated RhB@DiCH$_3$MOF-5 had been studied. There were no significant changes after 10 min ultrasonication, proving that ultrasonication would not change the MOF crystallinity. To further study the interaction of RhB dye and DiCH$_3$MOF-5 in the composite, time-resolved fluorescence decay experiments of both free RhB and RhB@DiCH$_3$MOF-5 composite were performed, respectively. According to Figure 2A and 2B, we can see that the

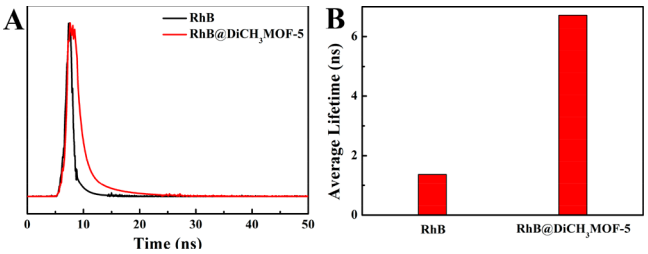

Figure 2. (A) Time-resolved fluorescence decay curves of RhB and RhB@DiCH$_3$MOF-5. (B) Comparison of fluorescence lifetime of free RhB molecules and RhB@DiCH$_3$MOF-5 composite.

fluorescence lifetime of RhB increased from 1.37 to 6.72 ns after being embedded into the pores of DiCH$_3$MOF-5. The increase of lifetime of RhB@DiCH$_3$MOF-5 was attributed to the decreased aggregation and deprotonation of RhB after encapsulation into the DiCH$_3$MOF-5 framework. The RhB@DiCH$_3$MOF-5 composite with prolonged lifetime provides a significant advantage for practical applications of RhB@DiCH$_3$MOF-5 in sensing.

Establishment of RhB@DiCH$_3$MOF-5-Based Sensor for Fe^{3+}. The kinetics of the sensing platform was first studied to understand the quenching rate of Fe^{3+} to RhB@DiCH$_3$MOF-5. As shown in Figure S7A, the fluorescence intensity of the RhB@DiCH$_3$MOF-5 dispersive solution decreased fast and gradually achieved fluorescence equilibrium after 10 min. This quenching rate can probably be attributed to the adsorption−diffusion of the porous structures of DiCH$_3$MOF-5 nanoparticles. The small-sized Fe^{3+} ions were first adsorbed on the NPs surface from the solution, followed by easy diffusion into the cavities of the RhB@DiCH$_3$MOF-5 probes, leading to a positive impact on the quenching kinetics. Thus, a 10 min cultivation time was chosen for the following experimental sensing studies to ensure the attainment of fluorescence quenching balance. The impact of different pH values on quenching was also assessed, and the results showed that this probe could selectively detect Fe^{3+} in NaAc−HAc buffer (10 mmol L^{-1}, pH 6.0) (Figure S7B). Figure 3A describes the changes of fluorescence intensity of the as-synthesized RhB@DiCH$_3$MOF-5 in the presence of different concentrations of Fe^{3+} (0, 1, 2, 3, 4, 5, 6, 7, 8, 9, 10, 30, 50, 70, 100, 300, 500, 700, and 1000 μmol L^{-1}). It can be seen that fluorescence decreases gradually as Fe^{3+} concentration increases. A linear relationship (R^2 = 0.9991) between fluorescence intensity and Fe^{3+} concentration in the range of 1−10 μmol L^{-1} was

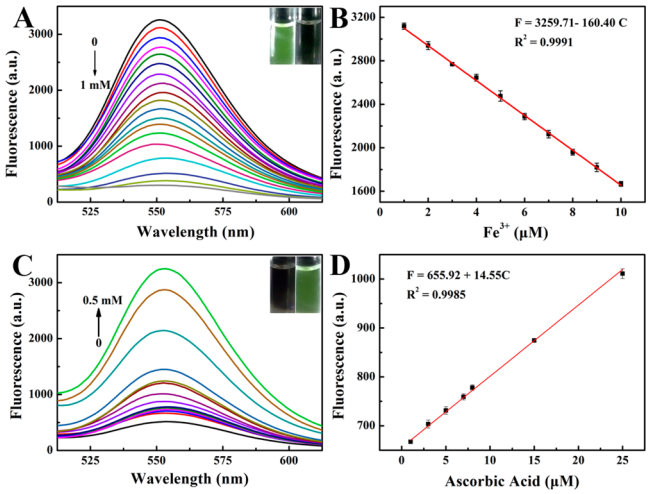

Figure 3. (A) Fluorescent spectra of RhB@DiCH$_3$MOF-5 (50 mg L^{-1}) under various concentrations of Fe^{3+}: 0, 1, 2, 3, 4, 5, 6, 7, 8, 9, 10, 30, 50, 70, 100, 300, 500, 700, and 1000 μmol L^{-1} from top to bottom. Inset shows the corresponding photos of RhB@DiCH$_3$MOF-5 in the absence (left) and presence of 1 mmol L^{-1} (right) Fe^{3+} under 365 nm UV light. (B) Standard curve for the determination of Fe^{3+} concentration. (C) Fluorescence emission spectra of RhB@DiCH$_3$MOF-5/Fe^{3+}-based sensor toward various concentrations of ascorbic acid: 0, 1, 3, 5, 7, 8, 15, 25, 50, 70, 80, 100, 300, and 500 μmol L^{-1} from bottom to top. Inset shows the corresponding photos of RhB@DiCH$_3$MOF-5/Fe^{3+} without (left) and with 1 mmol L^{-1} (right) ascorbic acid under 365 nm UV light. (D) Standard curve for the determination of ascorbic acid concentration.

achieved (Figure 3B). The limit of detection (LOD) was determined to be 0.36 μmol L^{-1} based on a signal-to-noise ratio of S/N = 3. The LOD obtained by the method reported herein is much lower than that of other reported fluorescence probes, demonstrating that the RhB@DiCH$_3$MOF-5 nanocrystals can be applied for efficient detection of Fe^{3+}.[8,42−44]

Selectivity is one of the most important factors when detecting metal ions in real complex samples. Therefore, selectivity tests were performed to evaluate the potential application of the RhB@DiCH$_3$MOF-5 composites. Various metal ions, including Na$^+$, K$^+$, Ni$^+$, Mg^{2+}, Ca^{2+}, Fe^{2+}, Co^{2+}, Cu^{2+}, Zn^{2+}, Mn^{2+}, Pb^{2+}, Ba^{2+}, Hg^{2+}, Al^{3+}, Cr^{3+}, and NH$_4^+$, were chosen to evaluate their influence on the fluorescence intensity of RhB@DiCH$_3$MOF-5 in the same conditions. When 16 different interference ions (1×10^{-4} mol L^{-1}) with concentrations of 10-fold of Fe^{3+} were added to the RhB@DiCH$_3$MOF-5 suspension, no obvious changes were observed in fluorescence intensity (Figure 4A). Only the addition of 1×10^{-5} mol L^{-1} Fe^{3+} to the above system showed significant quenching, indicating the superior selectivity of RhB@DiCH$_3$MOF-5 to Fe^{3+}. On the contrary, no such distinct selectivity or remarkable fluorescence quenching was observed when RhB@DiCH$_3$MOF-5 was replaced by free RhB molecules (Figure S8), demonstrating that the framework structure of DiCH$_3$MOF-5 played a vital role in the highly selective detection of Fe^{3+}.

Determination of Ascorbic Acid Based on RhB@DiCH$_3$MOF-5/Fe^{3+} Probe. Compared to Fe^{2+}, the high selectivity of RhB@DiCH$_3$MOF-5 to Fe^{3+} permitted the construction of a universal sensing platform for Fe^{3+} reductant detection. We assumed that the fluorescence of RhB would be recovered when Fe^{3+} was reduced to Fe^{2+}. To validate our assumption, ascorbic acid was selected to reduce Fe^{3+} to Fe^{2+}.

DOI: 10.1021/acs.analchem.9b03143
Anal. Chem. 2019, 91, 12453−12460

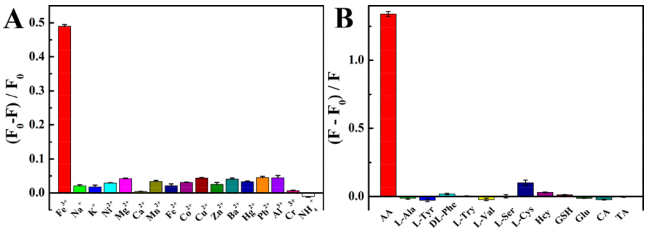

Figure 4. (A) Selectivity of RhB@DiCH$_3$MOF-5 (50 mg L^{-1}) for Fe^{3+} over other ions: concentration of Fe^{3+} was 1×10^{-5} mol L^{-1}; concentrations of other ions were all 1×10^{-4} mol L^{-1}. (B) Selectivity of RhB@DiCH$_3$MOF-5/Fe^{3+} for ascorbic acid over other interference substances: concentration of ascorbic acid was 50 μmol L^{-1}; concentrations of other interfering substances were all 500 μmol L^{-1}.

As shown in Figure S9, Fe^{3+} could be reduced to Fe^{2+} by ascorbic acid, whereas the reductive product, Fe^{2+}, had no significant influence on the fluorescence intensity of RhB@DiCH$_3$MOF-5. Thus, the quenched fluorescence of RhB@DiCH$_3$MOF-5/Fe^{3+} probe could be efficiently recovered upon addition of ascorbic acid. On the basis of these features, we designed a sensing platform to detect ascorbic acid using RhB@DiCH$_3$MOF-5/Fe^{3+} via a fluorescence "turn-on" response (Figure 3C). Moreover, we have optimized the concentration of Fe^{3+} in RhB@DiCH$_3$MOF-5/Fe^{3+} probe in detail. As shown in Figure S10A, the quenching efficiencies of RhB@DiCH$_3$MOF-5 were gradually increased after adding different concentrations of Fe^{3+} (0.1, 0.3, 0.5, 0.7, 1.0, 3.0, and 5.0 mmol L^{-1}). There is at least 85% fluorescence of RhB@DiCH$_3$MOF-5 quenching, as the concentration of Fe^{3+} was greater than 0.5 mmol L^{-1}. In addition, the sensitivity of ascorbic acid (10^{-4} mol L^{-1}) response to different concentrations of Fe^{3+} (0.1−5 mmol L^{-1}) were also investigated. From Figure S10B, the strongest fluorescence recovery occurred after adding 0.5 mmol L^{-1} Fe^{3+}. A larger Fe^{3+} concentration results in a higher fluorescence quenching efficiency, but excessive Fe^{3+} can cause poor response to ascorbic acid. Comprehensively, 0.5 mmol L^{-1} Fe^{3+} not only can obtain satisfactory quenching effect but can also show good sensitivity to ascorbic acid. Then the optimal Fe^{3+} concentration was determined to 0.5 mmol L^{-1}. Notably, without Fe^{3+} addition to the RhB@DiCH$_3$MOF-5 system, no obvious variation in fluorescence intensity was observed when only ascorbic acid was added (Figure S11), indicating that ascorbic acid does not affect this sensor.

The incubation time was also investigated to evaluate the fluorescence recovery rate upon adding ascorbic acid. The curve of fluorescence intensity versus incubation time is shown in Figure S12. Upon adding ascorbic acid, the fluorescence was recovered gradually and reached equilibrium after 30 min. This period of time was considered as the equilibrium time. As shown in Figure 3D, the fluorescence intensity of the RhB@DiCH$_3$MOF-5/Fe^{3+} system linearly increased as ascorbic acid concentration increased from 1 to 25 μmol L^{-1}. The correlation coefficient was determined to be R^2 = 0.9985, and the calculated LOD for ascorbic acid using the RhB@DiCH$_3$MOF-5/Fe^{3+} probe was determined to be 0.31 μmol L^{-1}, which is lower than the concentration of ascorbic acid in biological samples. Moreover, we further compare the performance of this platform with other reported MOFs or MOF composites for LOD, linear range, etc. (Table S1). As shown in Table S1, this newly developed sensor based on RhB@DiCH$_3$MOF-5 not only exhibits a long wavelength, a high sensitivity, and a comparable and lower LOD but can also simultaneously detect Fe^{3+} and ascorbic acid. In addition, the dye@MOF as a fluorescent probe to simultaneously determine Fe^{3+} and ascorbic acid in previous works has not been reported. Therefore, we hope this report can provide useful information for future analytical studies.

Along with sensitivity, the requirement of high selectivity is indispensable in most cases, especially in real sample detections. To study the specificity of the RhB@DiCH$_3$MOF-5/Fe^{3+} probe for ascorbic acid, some potential interference substances (L-Ala, L-Cys, GSH, L-Ser, L-Try, L-Tyr, L-Val, DL-Phe, Hcy, Glu, CA, and TA) were investigated under the same conditions, and the experimental results, as shown in Figure 4B, indicated that almost all interfering substances, even GSH, a biological reductase, had no obvious influence on the fluorescence intensity of RhB@DiCH$_3$MOF-5/Fe^{3+}. Collectively, therefore, we have demonstrated that our rationally designed fluorescent sensor has high detection selectivity and sensitivity to ascorbic acid and can be used to detect ascorbic acid in biological samples that contain interfering species.

Stability and Recyclability. There is no doubt that the stability of the probe is a vital factor in building a sensing platform. As shown in Figure S13, the morphology of RhB@DiCH$_3$MOF-5 was retained well after one circle detection, suggesting the relatively satisfactory stability of RhB@DiCH$_3$MOF-5. Moreover, we also investigated the reversible fluorescence of RhB@DiCH$_3$MOF-5 with addition of Fe^{3+} and ascorbic acid in turn (Figure S14). The fluorescence intensity of RhB@DiCH$_3$MOF-5 exhibits a strong fluorescence at about 550 nm and is quenched rapidly after adding Fe^{3+}. After addition of ascorbic acid, the fluorescence intensity of RhB@DiCH$_3$MOF-5 is recovered, and the fluorescence enhancement displays a good recovery in three consecutive cycles. The above data demonstrate that the established sensing platform, which can repeatedly detect Fe^{3+} and ascorbic acid at least three times, has good reversibility.

Analysis of Real Samples. To investigate the feasibility of the proposed method in real samples, RhB@DiCH$_3$MOF-5 was applied to determinate Fe^{3+} in human serum samples, and RhB@DiCH$_3$MOF-5/Fe^{3+} was applied to detect ascorbic acid in rat brain microdialysates.

Briefly, 100× diluted human serum samples were spiked with 3 μmol L^{-1}, 5 μmol L^{-1}, and 8 μmol L^{-1} of standard Fe^{3+} solution and measured according to the proposed method. As shown in Table S2, the recoveries were obtained in the range of 96.38−103.80%, and the relative standard deviation (RSD, n = 3) was less than 3%, demonstrating a high analytical precision of this sensor for monitoring Fe^{3+} in biological samples.

Further application of RhB@DiCH$_3$MOF-5/Fe^{3+} probe was evaluated using microdialysate of rat brain from the cortex region in the cerebral calm/ischemia condition. In a typical run, 100 μL of rat brain microdialysate was added to the sensing system, followed by measurement of fluorescence intensity. As shown in Figure 5, the basal level of cortical ascorbic acid was 3.62 ± 0.43 μmol L^{-1} within the calm period (60 min); then during surgical preischemia at around 20 min, the level of ascorbic acid in microdialysates slowly increased to 4.53 ± 0.57 μmol L^{-1} and presented a sustained trend of growth. Moreover, within 70 min after cerebral ischemia, the ascorbic acid level of the cortex region increased to 24.02 ± 2.10 μmol L^{-1}, a result consistent with previous studies.[35−38] Therefore, this probe could selectively differentiate ascorbic

DOI: 10.1021/acs.analchem.9b03143
Anal. Chem. 2019, 91, 12453−12460

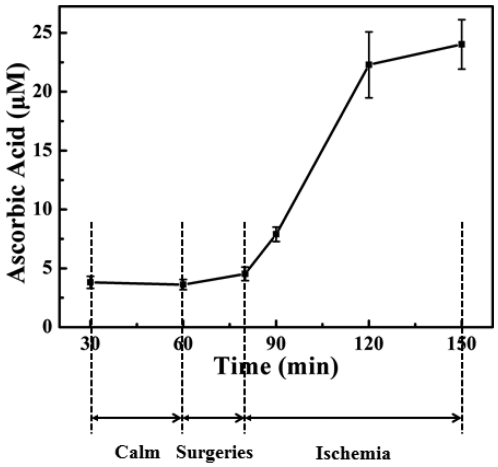

Figure 5. Ascorbic acid level in the rat brain microdialysates of the cortex region during different physiological conditions (0−60 min: calm; 60−80 min: surgeries; 80−150 min: ischemia).

acid from a number of potential interferences in biological fluids to, in turn, increase our understanding of the neurochemical process of cerebral ischemia.

Possible Mechanism for the Analysis of Fe^{3+} and Ascorbic Acid. We first studied the optical properties of Fe^{3+} and RhB@DiCH$_3$MOF-5 probe to understand the quenching mechanism. Figure 6A shows the absorption spectrum of Fe^{3+}

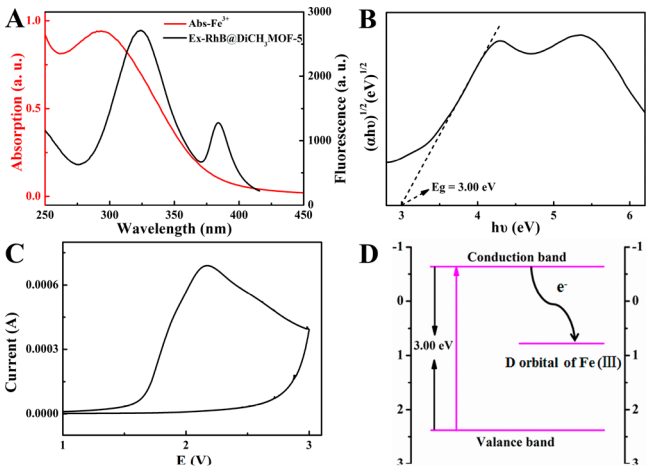

Figure 6. (A) UV−vis absorption spectra of Fe^{3+} (10^{-4} mol L^{-1}) and fluorescence excitation spectrum of RhB@DiCH$_3$MOF-5 (50 mg L^{-1}), respectively. (B) Plot of $(\alpha h\nu)^{1/2}$ vs photon energy (Eg) of RhB@DiCH$_3$MOF-5, and the dotted line is the linear fitting. (C) Cyclic voltammetry of RhB@DiCH$_3$MOF-5 composites in 10 mmol L^{-1} NaAc-HAc. (D) Principle scheme of PET mechanism between Fe^{3+} and RhB@DiCH$_3$MOF-5 composites.

and the fluorescence excitation spectrum of RhB@DiCH$_3$MOF-5. It is clear that Fe^{3+} has a strong absorption spectrum with a wide range from 260 to 400 nm, which overlapped with the excitation peak (325 nm) of RhB@DiCH$_3$MOF-5, thus enabling the generation of IFE between RhB@DiCH$_3$MOF-5 and Fe^{3+}. Meantime, fluorescence lifetime assay was carried out to further verify the fluorescence quenching mechanism. The fluorescence decay curves of RhB@DiCH$_3$MOF-5 without and with 10 μmol L^{-1} Fe^{3+} are shown in Figure S15. As shown in Figure S15, after adding 10 μmol L^{-1} Fe^{3+}, the fluorescence lifetime changes from 6.72 to 5.31 ns, which shows that the quenching mechanism is not just due to IFE because IFE is a static quenching process that does not cause perturbation of the excited state of the fluorophore.[45,46]

Meanwhile, synergistic quenching that stems from PET is another important factor in this sensor. To further explain this mechanism, we studied the electronic bandgap (E_g) and valence band (VB) of RhB@DiCH$_3$MOF-5 (Figure 6B and 6C). Based on the UV−vis absorption spectrum, the direct electronic bandgap of RhB@DiCH$_3$MOF-5 is about 3.00 eV by using a Tauc plot (Figure 6B). The oxidation potential of RhB@DiCH$_3$MOF-5 was determined to be 2.17 V against the Ag(s)/AgCl(s)/KCl (aq, satd) reference electrode, as shown in Figure 6C. Therefore, the VB and conduction band (CB) of RhB@DiCH$_3$MOF-5, using the electrochemical method, can be tested and calculated as

$$E_{\text{oxidation}} = 2.17 \text{ V versus Ag/AgCl/satd KCl}$$
$$= (2.17 + 0.20) \text{ V vs NHE}$$
$$= 2.37 \text{ V vs NHE}$$

Therefore, E_{VB} = 2.37 eV.

$$E_{VB} = 2.37 \text{ eV}, \quad E_g = 3.00 \text{ eV and } E_{CB} = E_{VB} - E_g$$

Therefore, E_{CB} = −0.63 eV.

Moreover, the electrode potential of Fe^{3+}/Fe^{2+} is 0.77 eV vs NHE, situated between CB and VB of RhB@DiCH$_3$MOF-5. When RhB@DiCH$_3$MOF-5 was irradiated, the electrons of VB were excited to CB and further transferred to the d orbit of Fe, resulting in the fluorescence of RhB@DiCH$_3$MOF-5 quenching through the PET (Figure 6D). Hence, Fe^{3+} can quench the fluorescence of RhB@DiCH$_3$MOF-5 based on the synergism between IFE and PET.

The fluorescence of RhB@DiCH3MOF-5 recovered after ascorbic acid was introduced to the quenched solution. The form of Fe^{3+} after the introduction of ascorbic acid into RhB@DiCH$_3$MOF-5/Fe^{3+} was investigated. 1,10-Phenanthroline was added into the RhB@DiCH$_3$MOF-5/Fe^{3+} and RhB@DiCH$_3$MOF-5/Fe^{3+} + ascorbic acid, and the photograph is shown in Figure S16. The RhB@DiCH$_3$MOF-5/Fe^{3+} + ascorbic acid in the presence of 1,10-phenanthroline presented an obvious color change compared to RhB@DiCH$_3$MOF-5/Fe^{3+}, which can be attributed to the orange-red complex of Fe^{2+} with 1,10-phenanthroline. That is to say, this fluorescence recovery could be attributed to an oxidation−reduction reaction. Moreover, we use two reducing organic acids (CA and TA) and three mercapto amino acids (L-Cys, Hcy, and GSH) as the interfering substance to verify its selectivity to ascorbic acid. The RhB@DiCH$_3$MOF-5/Fe^{3+} + ascorbic acid in the presence of 1,10-phenanthroline presented an obvious color change compared to RhB@DiCH$_3$MOF-5/Fe^{3+}. Furthermore, only the addition of L-Cys showed slight color change, which was consistent with our previous selectivity experiment study. This phenomenon may be attributed to the stronger reducing ability of ascorbic acid to Fe^{3+} compared with other interfering substances. In summary, the developed fluorescent switchable sensor showed acceptable selectivity for ascorbic acid and could be capable to detect ascorbic acid with the existence of interference species.

DOI: 10.1021/acs.analchem.9b03143
Anal. Chem. 2019, 91, 12453−12460

CONCLUSIONS

In summary, by embedding RhB into the porous crystalline $DiCH_3MOF$-5, we have developed an "on−off−on" MOF-regulated selective detection of Fe^{3+} and ascorbic acid in human serum and rat brain microdialysates. $DiCH_3MOF$-5 not only served as a regulator to selectively detection Fe^{3+} but also improved the photostability and the fluorescence lifetime of RhB. The simple one-pot synthesis approach of the RhB@$DiCH_3MOF$-5 nanoprobe has achieved low detection limits of Fe^{3+} and ascorbic acid in real biological samples. We believe this "on−off−on" MOF-regulated selective detection will provide insights into the design of MOF-based sensors for biochemical detections.

ASSOCIATED CONTENT

Supporting Information

The Supporting Information is available free of charge on the ACS Publications website at DOI: 10.1021/acs.analchem.9b03143.

The N_2 adsorption−desorption isotherms for $DiCH_3MOF$-5 and RhB@$DiCH_3MOF$-5, the chemical structure of RhB, the detailed spectra properties of RhB, $DiCH_3MOF$-5 and RhB@$DiCH_3MOF$-5, the SEM images of $DiCH_3MOF$-5 and RhB@$DiCH_3MOF$-5, the kinetics of RhB@$DiCH_3MOF$-5 response to Fe^{3+} and ascorbic acid, etc. (PDF)

AUTHOR INFORMATION

Corresponding Authors

*E-mail: xialian01@163.com.
*E-mail: fengliquhn@hotmail.com.

ORCID

Guang Chen: 0000-0002-0454-1686
Zhe Liu: 0000-0001-5796-4335
Fengli Qu: 0000-0001-6311-3051
Lian Xia: 0000-0001-6117-7596
Weihong Tan: 0000-0002-8066-1524

Author Contributions

All authors have given approval to the final version of the manuscript.

Notes

The authors declare no competing financial interest.

ACKNOWLEDGMENTS

This work is supported by grants awarded by the U.S. National Institutes of Health (nos. GM079359 and CA133086), the National Natural Science Foundation of China (nos. 21505084, 21775089, 21475074), Natural Science Foundation Projects of Shandong Province (nos. ZR2014BM029, ZR2013BQ019), Key Research and Development Program of Shandong Province (no. 2017GSF19109), and Innovation Project of Shandong Graduate Education (no. SDYY16091).

REFERENCES

(1) Guo, R. H.; Zhou, S. X.; Li, Y. C.; Li, X. H.; Fan, L. Z.; Voelcker, N. H. *ACS Appl. Mater. Interfaces* **2015**, *7*, 23958−23966.
(2) Nguyen Duc, T.; El Zein, R.; Raimundo, J. M.; Dallaporta, H.; Charrier, A. M. *J. Mater. Chem. B* **2013**, *1*, 443−446.
(3) Narayanaswamy, N.; Govindaraju, T. *Sens. Actuators, B* **2012**, *161*, 304−310.
(4) Zhang, S. W.; Li, J. X.; Zeng, M. Y.; Xu, J. Z.; Wang, X. K.; Hu, W. P. *Nanoscale* **2014**, *6*, 4157−4162.
(5) Ma, Q. Q.; Wang, J.; Li, Z. H.; Wang, D.; Hu, X. X.; Xu, Y. S.; Yuan, Q. *Inorg. Chem. Front.* **2017**, *4*, 1166−1172.
(6) Li, J. S.; Zhang, T. R.; Ge, J. P.; Yin, Y. D.; Zhong, W. W. *Angew. Chem., Int. Ed.* **2009**, *48*, 1588−1591.
(7) Ouyang, X. Y.; Yu, R. Q.; Jin, J. Y.; Li, J. S.; Yang, R. H.; Tan, W. H.; Yuan, J. L. *Anal. Chem.* **2011**, *83*, 782−789.
(8) Chen, W. D.; Gong, W. T.; Ye, Z. Q.; Lin, Y.; Ning, G. L. *Dalton Trans.* **2013**, *42*, 10093−10096.
(9) Lee, S.; Jang, H.; Lee, J.; Jeon, S. H.; Sohn, Y.; Ra, C. S. *Sens. Actuators, B* **2017**, *248*, 646−656.
(10) Shen, B. X.; Qian, Y. *Sens. Actuators, B* **2018**, *260*, 666−675.
(11) Wang, B. D.; Hai, J.; Liu, Z. C.; Wang, Q.; Yang, Z. Y.; Sun, S. H. *Angew. Chem., Int. Ed.* **2010**, *49*, 4576−4579.
(12) Guo, X. R.; Yue, G. Q.; Huang, J. Z.; Liu, C.; Zeng, Q.; Wang, L. S. *ACS Appl. Mater. Interfaces* **2018**, *10*, 26118−26127.
(13) Liu, Y. H.; Duan, W. X.; Song, W.; Liu, J. J.; Ren, C. L.; Wu, J.; Liu, D.; Chen, H. L. *ACS Appl. Mater. Interfaces* **2017**, *9*, 12663−12672.
(14) Shangguan, J. F.; Huang, J.; He, D. G.; He, X. X.; Wang, K. M.; Ye, R. Z.; Yang, X.; Qing, T. P.; Tang, J. L. *Anal. Chem.* **2017**, *89*, 7477−7484.
(15) Shi, B. F.; Su, Y. B.; Zhang, L. L.; Huang, M. J.; Liu, R. J.; Zhao, S. L. *ACS Appl. Mater. Interfaces* **2016**, *8*, 10717−10725.
(16) Cui, Y. J.; Xu, H.; Yue, Y. F.; Guo, Z. Y.; Yu, J. C.; Chen, Z. X.; Gao, J. K.; Yang, Y.; Qian, G. D.; Chen, B. L. *J. Am. Chem. Soc.* **2012**, *134*, 3979−3982.
(17) Deng, J. J.; Wang, K.; Wang, M.; Yu, P.; Mao, L. Q. *J. Am. Chem. Soc.* **2017**, *139*, 5877−5882.
(18) Guo, L.; Liu, Y.; Kong, R. M.; Chen, G.; Wang, H.; Wang, X. L.; Xia, L.; Qu, F. L. *Sens. Actuators, B* **2019**, *295*, 1−6.
(19) Morris, W.; Briley, W. E.; Auyeung, E.; Cabezas, M. D.; Mirkin, C. A. *J. Am. Chem. Soc.* **2014**, *136*, 7261−7264.
(20) Li, Z. P.; Zhang, Y. W.; Xia, H.; Mu, Y.; Liu, X. M. *Chem. Commun.* **2016**, *52*, 6613−6616.
(21) Wang, S. Z.; McGuirk, M.; Ross, M. B.; Wang, S. Y.; Chen, P. C.; Xing, H.; Liu, Y.; Mirkin, C. A. *J. Am. Chem. Soc.* **2017**, *139*, 9827−9830.
(22) Liu, X. M.; Xu, Y. H.; Jiang, D. L. *J. Am. Chem. Soc.* **2012**, *134*, 8738−8741.
(23) Wang, K.; Li, N.; Zhang, J.; Zhang, Z. Q.; Dang, F. Q. *Biosens. Bioelectron.* **2017**, *87*, 339−344.
(24) Hou, S. L.; Dong, J.; Jiang, X. L.; Jiao, Z. H.; Wang, C. M.; Zhao, B. *Anal. Chem.* **2018**, *90*, 1516−1519.
(25) Yang, C. X.; Ren, H. B.; Yan, X. P. *Anal. Chem.* **2013**, *85*, 7441−7446.
(26) Qi, Z. W.; Chen, Y. *Biosens. Bioelectron.* **2017**, *87*, 236−241.
(27) Wang, C.; Wang, J. L.; Lin, W. B. *J. Am. Chem. Soc.* **2012**, *134*, 19895−19908.
(28) Yang, J.; Dai, Y.; Zhu, X. Y.; Wang, Z.; Li, Y. S.; Zhuang, Q. X.; Shi, J. L.; Gu, J. L. *J. Mater. Chem. A* **2015**, *3*, 7445−7452.
(29) Yang, D. D.; Tian, Y.; Xu, W. L.; Cao, X. W.; Zheng, S. J.; Ju, Q.; Huang, W.; Fang, Z. L. *Inorg. Chem.* **2017**, *56*, 2345−2353.
(30) Zhou, Y.; Chen, H. H.; Yan, B. *J. Mater. Chem. A* **2014**, *2*, 13691−13697.
(31) Hou, S. L.; Dong, J.; Tang, M. H.; Jiang, X. L.; Jiao, Z. H.; Zhao, B. *Anal. Chem.* **2019**, *91*, 5455−5460.
(32) Song, T. Q.; Yuan, K.; Qiao, W. Z.; Shi, Y.; Dong, J.; Gao, H. L.; Yang, X. P.; Cui, J. Z.; Zhao, B. *Anal. Chem.* **2019**, *91*, 2595−2599.
(33) Xu, H.; Hu, H. C.; Cao, C. S.; Zhao, B. *Inorg. Chem.* **2015**, *54*, 4585−4587.
(34) Yang, J.; Grzech, A.; Mulder, F. M.; Dingemans, T. J. *Chem. Commun.* **2011**, *47*, 5244−5246.
(35) Li, L. B.; Wang, C.; Liu, K. Y.; Wang, Y. H.; Liu, K.; Lin, Y. Q. *Anal. Chem.* **2015**, *87*, 3404−3411.
(36) Kong, W. H.; Wu, D.; Li, G. L.; Chen, X. F.; Gong, P. W.; Sun, Z. W.; Chen, G.; Xia, L.; You, J. M.; Wu, Y. N. *Talanta* **2017**, *165*, 677−684.

DOI: 10.1021/acs.analchem.9b03143
Anal. Chem. 2019, 91, 12453−12460

(37) Liu, K.; Lin, Y. Q.; Yu, P.; Mao, L. Q. *Brain Res.* **2009**, *1253*, 161−168.
(38) Zhang, M. N.; Liu, K.; Gong, K. P.; Su, L.; Chen, Y.; Mao, L. Q. *Anal. Chem.* **2005**, *77*, 6234−6242.
(39) Lv, Y. Q.; Yu, H. T.; Xu, P. C.; Xu, J. Q.; Li, X. X. *Sens. Actuators, B* **2018**, *256*, 639−647.
(40) Yu, J. C.; Cui, Y. J.; Xu, H.; Yang, Y.; Wang, Z. Y.; Chen, B. L.; Qian, G. D. *Nat. Commun.* **2013**, *4*, 2719.
(41) Abdelhamid, H. N.; Huang, Z. H.; El-zohry, A. M.; Zheng, H. Q.; Zou, X. D. *Inorg. Chem.* **2017**, *56*, 9139−9146.
(42) Atchudan, R.; Edison, T. N. J. I.; Aseer, K. R.; Perumal, S.; Karthik, N.; Lee, Y. R. *Biosens. Bioelectron.* **2018**, *99*, 303−311.
(43) He, L.; Li, J. N.; Xin, J. H. *Biosens. Bioelectron.* **2015**, *70*, 69−73.
(44) Song, Y.; Zhu, C. Z.; Song, J. H.; Li, H.; Du, D.; Lin, Y. H. *ACS Appl. Mater. Interfaces* **2017**, *9*, 7399−7405.
(45) Zhu, X. H.; Zhao, T. B.; Nie, Z.; Liu, Y.; Yao, S. Z. *Anal. Chem.* **2015**, *87*, 8524−8530.
(46) Kong, W. H.; Wu, D.; Xia, L.; Chen, X. F.; Li, G. L.; Qiu, N. N.; Chen, G.; Sun, Z. W.; You, J. M.; Wu, Y. N. *Anal. Chim. Acta* **2017**, *973*, 91−99.

DOI: 10.1021/acs.analchem.9b03143
Anal. Chem. 2019, 91, 12453−12460